



photonics [14], neuromorphic computing [22, 23], Internet of Things (IoT) [24], and machine learning [25]. Silicon nitride (SiN<sub>x</sub>) is one of the three currently commercially viable photonic platforms [26], the other two being silicon [27] and indium phosphide [28, 29]. SiN<sub>x</sub> provides an alternative low-cost CMOS compatible platform and similar to the silicon platform all fundamental non amplifying photonic components can be implemented [30]. The advantages over Si are fabrication flexibility, low temperature processing (<400 °C), refractive index tunability, high transparency and low temperature sensitivity [31]. As a result, SiN<sub>x</sub> waveguides have been widely employed for light propagation in the mid infrared, the near infrared and in the visible range of the electromagnetic spectrum [32, 33]. The versatility of the SiN<sub>x</sub> platform is key in the implementation of complex multi-layer photonic circuitry. The reduced mode confinement compared to Si, allows for compact active regions of programmable devices reducing the energy required to switch them [34, 35]. Phase change materials (PCMs) are being extensively studied for their use in photonic integrated circuits as they offer high refractive index contrast and are non-volatile. Benefiting from prior art such as rewritable optical media and resistive memories, the mature technology of chalcogenide PCMs are now seen as a promising CMOS compatible route to provide the much needed non-volatile re-configurability in integrated photonics [36]. PCMs have the ability to switch between two states, an amorphous and a crystalline phase with a resulting large optical contrast (allowing also intermediate states of crystallization). They are stable (years at room temperature) [37–39], can be switched between states rapidly (nanoseconds or less) [40, 41], and exhibit high endurance (number of switching cycles) [42, 43]. The fundamental advantage of PCM-based programmable circuits compared to the conventional thermo-optic based approach is that energy is only consumed during the actual switching process. PCM-based devices have been demonstrated in a variety of applications such as switches [44, 45], wavelength division multiplexers [46], directional couplers [47], memories [46, 48–50] and neuromorphic devices [51, 52]. Most PCM-based devices to date make use of the well-known pseudo-binary phase change material Ge<sub>2</sub>Sb<sub>2</sub>Te<sub>5</sub> (GST). Although it is established as a mature technology, GST was designed to offer fast switching (ns) and stability for applications that employ changes in reflectivity through the refractive index contrast, as applied in the CD, DVD, etc, or resistivity differences, applications which are largely independent on optical loss. On the other hand, PICs that employ GST present strong coupling between amplitude and phase modulation due to the high absorption of the crystalline phase of the material. This coupling severely reduces the potential modulation schemes while it limits systems to a small number of components due to inherent losses.

Emerging applications such as quantum information have been deemed viable ought to photonic integration but the vast computational requirements demand large systems prohibitive to lossy mediums. Even though GST-225 offers low losses 0.039 dB/μm in the amorphous state, the crystalline phase presents losses as high as 2.7 dB/μm at 1550 nm [53]. Addition of selenium to GST (GSST) presents an alternative solution to non-volatile low-loss phase change materials for photonic integrated circuits and different building blocks have been experimentally fabricated and tested. A low-loss directional coupler on a silicon platform has been demonstrated with losses as low as 0.083 dB [45]. Integrating GSST on a silicon nitride platform, a ring resonator switch has been experimentally measured in [54] with losses of 0.2 dB and an extinction ratio of 41 dB. Also, a hybrid phase change material GSST-silicon Mach Zehnder modulator, with low insertion loss (3 dB), to serve as node in a photonic neural network has been demonstrated in [55]. Finally, a family of broadband transparent optical phase change materials for high-performance non-volatile photonics was explored in [56]. These materials still maintain a relatively high loss (extinction coefficient) in order to switch the PCM optically. A novel family of low-loss PCMs which includes Sb<sub>2</sub>S<sub>3</sub> and Sb<sub>2</sub>Se<sub>3</sub> has been recently shown [57, 58] and devices taking advantage of their optical properties such as Bragg gratings [59] and ring resonators [60] have been demonstrated. Sb<sub>2</sub>S<sub>3</sub> was first proposed in [57], while [58] introduced improvements by optimising the deposition

conditions of  $\text{Sb}_2\text{S}_3$  and by achieving repeatable switching durability. More importantly, Delaney et al. [58] showed that  $\text{Sb}_2\text{Se}_3$ , in which sulfur is completely substituted by selenium, offers an equally low-loss alternative at lower switching temperatures.  $\text{Sb}_2\text{S}_3$  offers a refractive index contrast ( $\Delta n$ ) between its states of 0.60 at 1550 nm and 0.58 at 1310 nm, while for  $\text{Sb}_2\text{Se}_3$ ,  $\Delta n=0.77$  at 1550 nm and 0.82 at 1550 nm. Both materials present low inherent losses since their extinction coefficient,  $k$  is less than  $10^{-4}$  in both phases at 1550 nm and at 1310 nm. The crystallisation temperature has been found to be 290 °C for  $\text{Sb}_2\text{S}_3$  and 190 °C for  $\text{Sb}_2\text{Se}_3$ . Hence,  $\text{Sb}_2\text{Se}_3$  is easier to switch due to its lower crystallisation temperature while the lower bandgap energy of 1.48 eV compared to the 1.98 eV of  $\text{Sb}_2\text{S}_3$  results in a shifted absorption spectrum towards higher wavelengths. As a result, the favourable properties of both materials cover a range of applications. In this paper, we integrate these novel low-loss PCM materials with a silicon nitride integrated platform to demonstrate their high performance in phase modulation. We employ MZIs and use the effective refractive index contrast and absorption as metrics to assess their operation at two different wavelengths, 1310 nm and 1550 nm.

## 2. Fabrication and characterization

Silicon nitride Mach-Zehnder interferometers (MZIs) were fabricated exploiting the novel low loss phase change materials,  $\text{Sb}_2\text{S}_3$  and  $\text{Sb}_2\text{Se}_3$  to utilize them as non-volatile phase modulators building blocks. The MZIs building block structures were designed in order to test the performance of both  $\text{Sb}_2\text{S}_3$  and  $\text{Sb}_2\text{Se}_3$  incorporated in the proposed silicon nitride platform at both 1310 nm and 1550 nm wavelengths. These devices were fabricated on 8" Si wafers with a 2  $\mu\text{m}$  thermally-grown  $\text{SiO}_2$  on top of which a 300 nm  $\text{SiN}_x$  layer ( $n = 2.0$ ) was deposited at 350 °C using the  $\text{NH}_3$  PECVD process fully detailed in [61]. The test structures were defined on the wafers by means of 248 nm deep-UV (DUV) lithography and the pattern was transferred onto the  $\text{SiN}$  layer using inductively coupled plasma etching (ICP) with an etch depth of 300 nm forming ridge structures. The PCMs were deposited through windows defined by the second DUV lithography step. The PCM deposition was performed by RF sputtering as described in [58]. A 10 nm  $\text{ZnS}/\text{SiO}_2$  capping layer was deposited by sputtering right after the deposition of the PCM. The photoresist was lift-off by sequentially dipping in room temperature acetone and 80 °C NMP with ultrasonic agitation. After rinsing in acetone, IPA and drying with a nitrogen gun a second 10 nm layer of  $\text{ZnS}/\text{SiO}_2$  was deposited to provide further protection of the exposed interfaces.

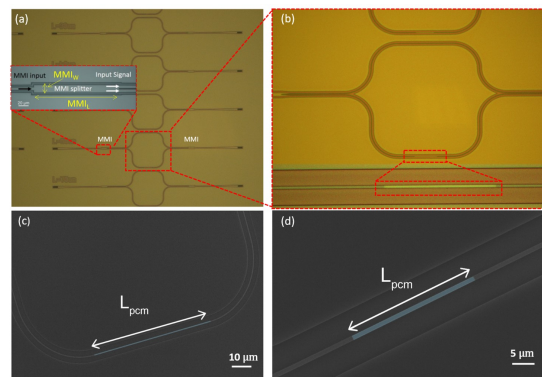


Fig. 1. Optical microscope and SEM images of the fabricated structures. (a) MZIs using different cell lengths. (b) Zoom in image of (a) with an inset of the PCM deposited layer. (c) SEM image of the longer arm of the MZI with the cell deposited on top. (d) Zoom in SEM image of a PCM cell with fake color

The layout we designed included a set of 12 MZIs with single-mode waveguide cross-sections of  $1.2 \times 0.3 \mu\text{m}^2$  for 1550 nm (C-band) and  $0.9 \times 0.3 \mu\text{m}^2$  for 1310 nm (O-band). These MZIs have an optical path length difference of  $\Delta L = 60 \mu\text{m}$  at 1310 nm and  $\Delta L = 40 \mu\text{m}$  at 1550 nm between their arms, see Fig. 1(a). In the longer arm of the MZI, PCM cells with a thickness of  $(20 \pm 4)$  nm for  $\text{Sb}_2\text{S}_3$  and  $(15 \pm 4)$  nm for  $\text{Sb}_2\text{Se}_3$  and different lengths ranging from 2-125  $\mu\text{m}$  were deposited. To split and combine the light, 3 dB broadband multi-mode interferometers (MMIs) were employed, see inset of Fig 1(a). The dimensions of the MMI at  $\lambda = 1.31 \mu\text{m}$ , were  $\text{MMI}_L = 41 \mu\text{m}$  and  $\text{MMI}_W = 9 \mu\text{m}$ , and respectively for  $\lambda = 1.55 \mu\text{m}$ ,  $\text{MMI}_L = 64 \mu\text{m}$  and  $\text{MMI}_W = 11 \mu\text{m}$ . SEM images of the longer MZI arm were taken with different lengths of the PCM cell. In Figure 1(c), a cell length of a 100  $\mu\text{m}$  was captured and in Fig. 1(d) a zoom in image of the longer arm with a cell length of 20  $\mu\text{m}$  was measured. All the devices included input and output grating couplers (GCs) designed to couple the light at either of both wavelengths of interest for characterisation, 1310 or 1550 nm. The GCs designed for 1310 nm consisted of a  $10 \mu\text{m} \times 37 \mu\text{m}$  surface grating with a period of 1038 nm tapered down to a single-mode waveguide width of 900 nm, whereas the ones designed for 1550 nm had a surface grating with the same dimensions and a period of 1238 nm tapered to a single-mode width of 1200 nm. The angle between the optical fibers delivering light and the gratings was selected to be  $10^\circ$  or  $15^\circ$  to the normal to ensure maximum coupling at 1310 or 1550 nm, respectively. Additionally, the layout included separate structures with two GCs connected back-to-back for normalisation purposes. The spectral response for all the devices was characterised using two different tunable laser sources. An Agilent 8163B Lightwave Multimeter for the response at 1550 nm and a similar Agilent 8164B Lightwave Measurement System for the response at 1310 nm. The measurements were first performed for the amorphous state of the PCMs and then for their crystalline state. The phase change was induced thermally by heating the chip on a hot plate at the crystallisation temperature for 10 minutes. In both cases, the polarization of the light was controlled to ensure that only TE modes could propagate through the devices and the measurements were normalized to extract the loss contribution of the grating couplers.

### 3. Results and discussion

Silicon nitride MZIs were fabricated using novel low loss phase change materials,  $\text{Sb}_2\text{S}_3$  and  $\text{Sb}_2\text{Se}_3$  to demonstrate a low-loss non-volatile MZI building block for future electro-refractive non-volatile photonic integrated circuit applications in the O and C-bands. Firstly, the  $\text{Sb}_2\text{S}_3$  material is analysed. The bare MZI structure without phase change material was characterized and normalized with respect to GCs connected back-to-back. Afterwards, the response of the MZIs for different lengths of the PCM cell were characterized in both amorphous (Fig. 2(a) and (c)) and crystalline states (Fig. 2(b) and (d)) at both target wavelengths.

In Fig. 2(a), the bare MZI presents a free-spectral range (FSR) of 13 nm in the O-band. Only cell lengths of 10, 20 and 30  $\mu\text{m}$  were selected to be plotted in order to not overload the graph with all the cell lengths used in the study. The shift in wavelength ( $\Delta\lambda$ ) produced by the cell lengths were 2.75, 4.38 and 9.47 nm respectively in the amorphous state respect to the bare MZI. In Fig. 2(b), the crystalline state is shown in the O-band. For the bare structure after crystallization, the FSR maintained the previous value (prior to crystallization), even though a shift has been produced in the dips of the optical spectrum due to the crystallization process to which the chip was submitted. In this case, a shift in wavelength for the cells of length 10, 20 and 30  $\mu\text{m}$  of 7.64, 9.5 and 13.03 nm, respectively, was measured.

In each case, an extinction ratio (ER) higher than 20 dB is shown for the different MZI structures. Fig 2(c) represents the MZI response using  $\text{Sb}_2\text{S}_3$  in the amorphous state of the PCM in the C-band. A FSR of 31 nm was extracted, higher than the one measured in the O-band (13 nm), a shift in wavelength for cell lengths of 10, 15 and 20  $\mu\text{m}$  of 9.67, 12.76 and 16.07 nm was experimentally demonstrated. In Fig 2(d), the crystalline state of the PCM for the C-band

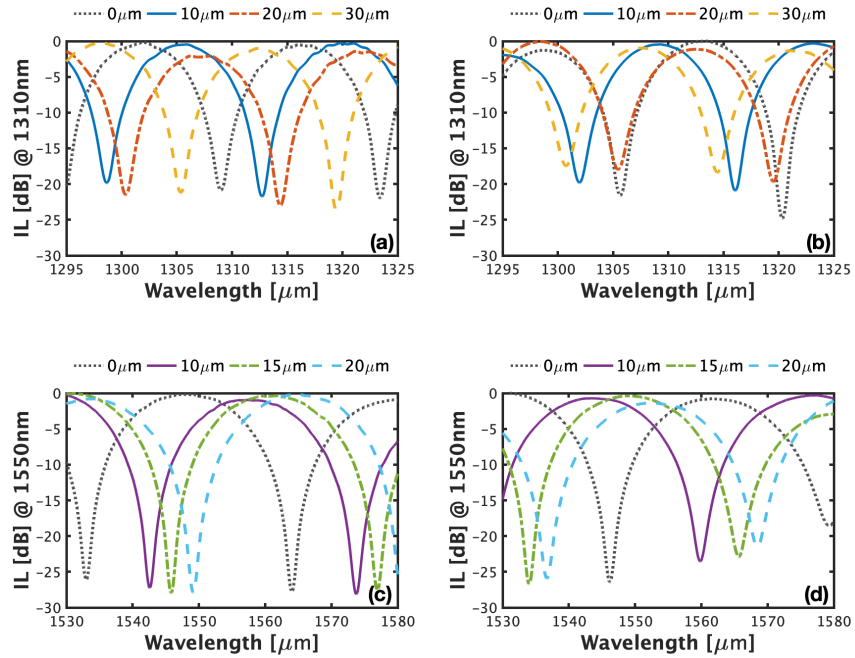


Fig. 2. MZI response for different cell lengths, as indicated in the legends, of  $\text{Sb}_2\text{S}_3$  in the (a) amorphous state at 1310 nm, (b) crystalline state at 1310 nm, (c) amorphous state at 1550 nm and (d) crystalline state at 1550 nm.

is shown and shifts of 13.5, 19.5 and 22.5 nm were obtained for the three different cell lengths, 10, 15 and 20  $\mu\text{m}$ . ERs as high as 30 dB were experimentally demonstrated in this range of the spectrum, achieving a difference of 7.64, 9.5 and 13.03 nm for the O-band and respectively 3.83, 6.74 and 6.43 nm for the C-band between crystalline and amorphous dips.

Afterwards, we characterized the insertion loss (IL) introduced by the PCM layer ( $\alpha$ ) and the modulation in effective refractive index ( $\Delta n_{eff}$ ) in its amorphous and crystalline states. The IL and the modulation in phase were extracted from the spectral response of the fabricated MZIs. To characterize the losses of the PCM cell, the ER of each individual MZI with the corresponding cell length was evaluated and consequently the loss coefficient extracted using the equation from Ref. [62]:

$$ER = \left( \frac{1 + e^{-\frac{\alpha L_{pcm}}{2}}}{1 - e^{-\frac{\alpha L_{pcm}}{2}}} \right)^2 \quad (1)$$

where  $L_{pcm}$  is the length of the PCM cell. For the amorphous state of the PCM, the ER was not varying significantly while increasing the cell length, showing a low loss introduced by the PCM in both ranges of the spectrum. The extracted losses in the amorphous state for the wavelengths of interest are lower than  $10^{-4}$  dB/ $\mu\text{m}$ . For the crystalline state, ERs were decreasing with increasing the cell lengths, showing an increment in losses in the crystalline state respect to the amorphous state. The measured IL in the crystalline state, were as low as  $(0.031 \pm 0.003)$  dB/ $\mu\text{m}$  and  $(0.023 \pm 0.005)$  dB/ $\mu\text{m}$  at 1310 nm and 1550 nm respectively, see Fig. 3.

Once the IL of the PCM was characterized, the effective refractive index modulation of the material can be obtained using the equation from Ref. [63]:

$$\Delta n_{eff}^{(a-c)} = \frac{\lambda}{FSR} \cdot \frac{\Delta\lambda^{(a-c)}}{L_{pcm}} \quad (2)$$

where  $\Delta n_{eff}$  is the variation produced in the effective refractive index when the PCM cell is introduced compared to the bare structure (no PCM), the superscripts  $a$  and  $c$  refer to the amorphous and crystalline states respectively, FSR is the free spectral range as previously introduced, and  $\Delta\lambda$  is the shift in the dip of the amorphous and crystalline states with respect to the dip produced by the bare MZI waveguide as introduced previously. Figure 4 shows the  $\Delta n_{eff}$  for both ranges of the spectrum, 1310 nm (Fig. 4(a)) and 1550 nm (Fig. 4(b)). The modulation between the amorphous state and the bare waveguide, the crystalline state and the bare waveguide and the amorphous state compared with the crystalline state ( $\Delta$ ) are presented in Fig. 4. The overall effective refractive index contrast between amorphous and crystalline states was measured to be 0.05 and 0.02 at 1310 nm and 1550 nm, respectively.

The same procedure was used in order to characterize the building block performance of the MZIs devices for the material,  $Sb_2Se_3$ . In this case, the spectral response for the different MZIs is presented in Fig. 5. Fig 5(a) shows the amorphous state of the  $Sb_2Se_3$  material in the O-band. A shift of 9, 15.5 and 25.4 nm between the bare MZI dip and the MZI dip with PCM cells of 10, 20 and 30  $\mu m$  was measured respectively. For the crystalline state, an increase in the shift is produced compared with the amorphous state and a shift of 13, 17.9 and 31.5 nm is measured for cell lengths of 10, 20 and 30  $\mu m$  respectively. In all the cases ERs higher than 20 dB were demonstrated, see Fig. 5(b). In the C-band, the  $Sb_2Se_3$  material showed a modulation in wavelength of 10.3, 17.5 and 24.9 nm for PCM amorphous cell lengths of 5, 10 and 15  $\mu m$ .

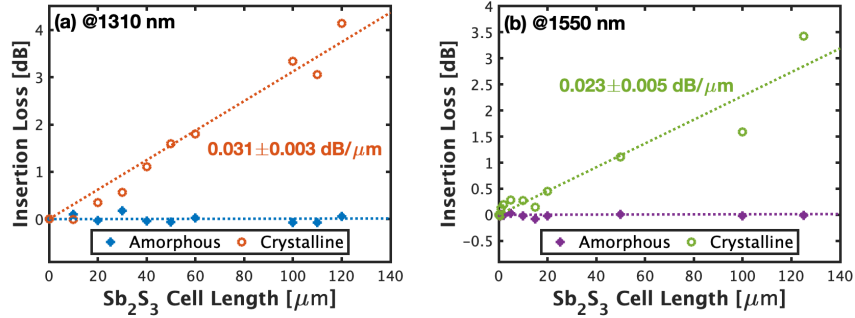


Fig. 3. Measured losses for different cell lengths of  $Sb_2S_3$  in both amorphous and crystalline state at (a) 1310 nm and (b) 1550 nm.

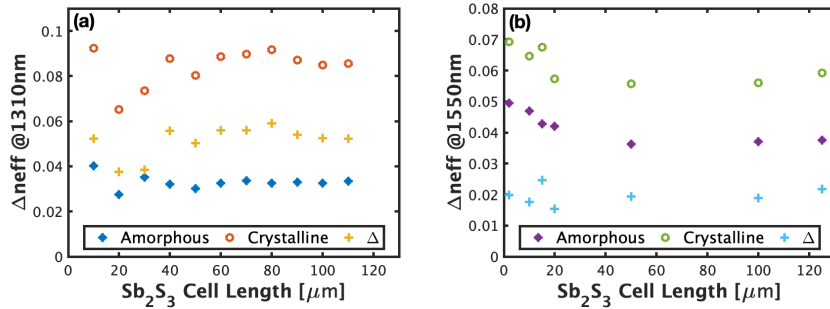


Fig. 4. Effective refractive index difference ( $\Delta n_{eff}$ ) as a function of cell length for both amorphous and crystalline states of  $Sb_2S_3$  at (a) 1310 nm and (b) 1550 nm.

When switching to crystalline state, the modulation is 14.9, 30.65 and 41.4 nm respectively, see Fig. 5(c-d). Resulting in a  $\Delta\lambda$  of 4, 2.1 and 6.1 nm for O-band and respectively 4.6, 13.15 and 16.5 nm for the C-band.

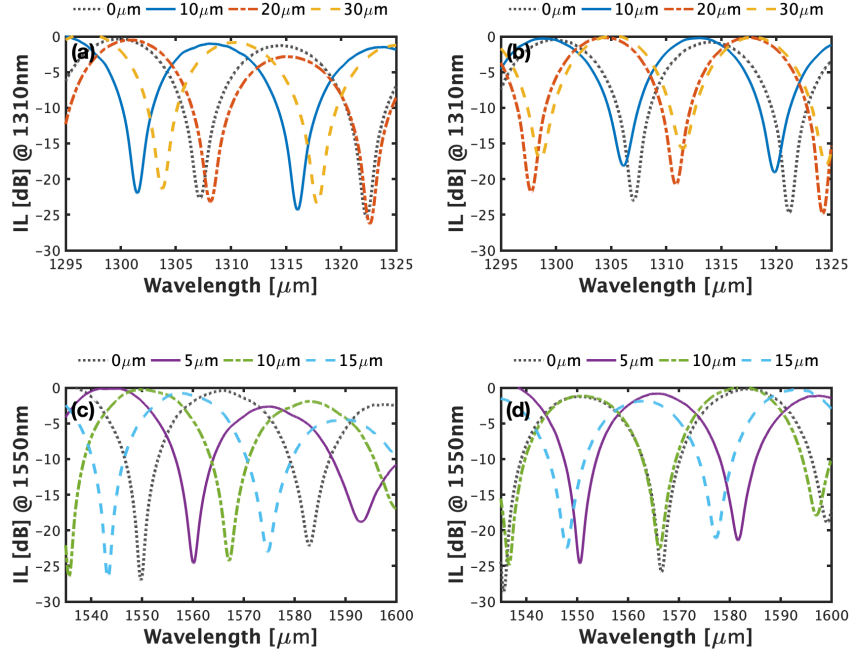


Fig. 5. MZI response for different cell lengths, as indicated in the legends, of  $\text{Sb}_2\text{Se}_3$  in the (a) amorphous state at 1310 nm, (b) crystalline state at 1310 nm, (c) amorphous state at 1550 nm and (d) crystalline state at 1550 nm.

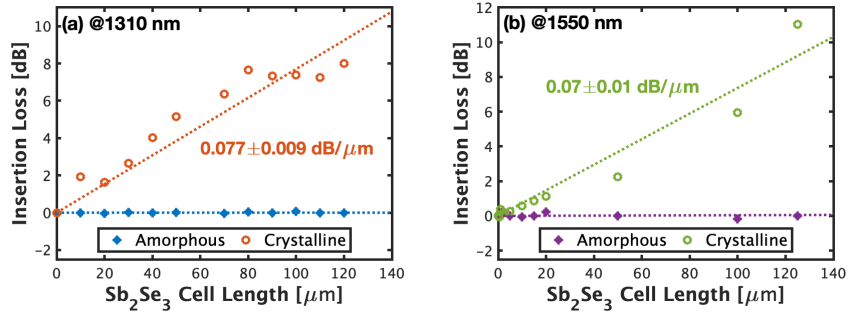


Fig. 6. Measured losses for different cell lengths of  $\text{Sb}_2\text{Se}_3$  in both amorphous and crystalline state at (a) 1310 nm and (b) 1550 nm.

The ILs and the effective index modulation were extracted using the same method used for the  $\text{Sb}_2\text{S}_3$  material. In this case, the measured losses in both states are shown in Fig. 6. In the amorphous state of  $\text{Sb}_2\text{Se}_3$  for the wavelengths of interest, losses are lower than  $10^{-4} \text{ dB}/\mu\text{m}$ , whereas in the crystalline state, losses are  $(0.077 \pm 0.009) \text{ dB}/\mu\text{m}$  at 1310 nm and  $(0.07 \pm 0.01) \text{ dB}/\mu\text{m}$  at 1550 nm. The effective refractive index difference between the amorphous and crystalline state was measured to be 0.03 at 1310 nm and 0.05 at 1550 nm as shown in Fig. 7.

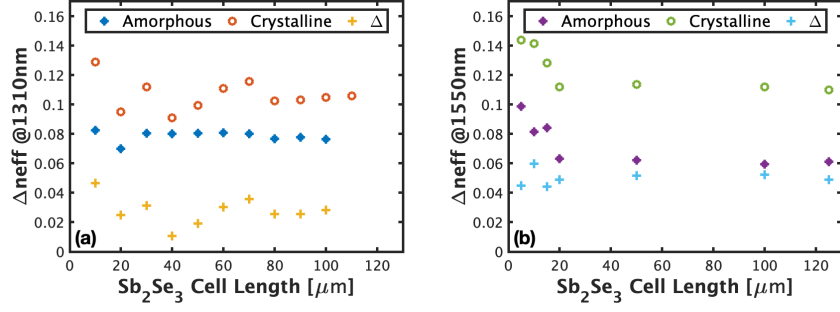


Fig. 7. Effective refractive index difference ( $\Delta n_{eff}$ ) as a function of cell length for both amorphous and crystalline states of  $Sb_2Se_3$  at (a) 1310 nm and (b) 1550 nm.

Table 1 presents the optical performance of the currently popular phase change materials GST, GSST and the novel materials discussed in this paper,  $Sb_2S_3$  and  $Sb_2Se_3$  on our integrated silicon nitride platform. In the table, a comparison of the cell length required in order to achieve a  $\pi$  shift ( $L_\pi = \lambda/2 \cdot (\Delta n_{eff})$ ) and the IL that this cell introduces in the device are also shown. GST offers a  $\pi$  phase shift at the shortest length while GSST requires double,  $Sb_2Se_3$  triple and  $Sb_2S_3$  seven times that length (the GST length) for the same shift at 1550 nm. However, the popularity of GSST stems from the three times lower insertion loss when compared to GST. Our  $Sb_2Se_3$  and  $Sb_2S_3$  films offer a stark improvement with the insertion loss at 13 and 18 times lower than GST respectively, significantly surpassing the benefits of GSST. In the O-band (1310 nm), the required length for a  $\pi$  shift ( $L_\pi$ ) in the case of  $Sb_2Se_3$  is 21.83  $\mu m$ , although, there is a reduction of 12.5  $\mu m$  for GST, 14.5  $\mu m$  for GSST and 9  $\mu m$  for the  $Sb_2S_3$  material. Again in this range of the spectrum the IL introduced by the novel materials highly improve the performance of GST and GSST. It is therefore obvious that both materials provide in the O band and C band an incontestable improvement on insertion losses compared with GST and GSST in the crystalline state.

PCM	C-band @ 1550 nm					O-band @ 1310 nm				
	$\alpha_c$ [dB/ $\mu m$ ]	$\alpha_a$ [dB/ $\mu m$ ]	$\Delta n_{eff}$	$L_\pi$ [ $\mu m$ ]	IL $_\pi$ [dB]	$\alpha_c$ [dB/ $\mu m$ ]	$\alpha_a$ [dB/ $\mu m$ ]	$\Delta n_{eff}$	$L_\pi$ [ $\mu m$ ]	IL $_\pi$ [dB]
GST [53]	2.860	0.039	0.14	5.53	15.81	6.660	0.228	0.07	9.36	62.4
GSST* [59]	0.53	$<10^{-4}$	0.074	10.5	5.56	1.42	$<10^{-4}$	0.09	7.28	10.3
$Sb_2S_3$	$0.023 \pm 0.005$	$<10^{-4}$	0.02	38.75	0.89	$0.031 \pm 0.003$	$<10^{-4}$	0.05	13.1	0.39
$Sb_2Se_3$	$0.07 \pm 0.01$	$<10^{-4}$	0.05	15.5	1.15	$0.077 \pm 0.009$	$<10^{-4}$	0.03	21.83	1.68

Table 1. The device performance comparison between the C-band (1550 nm) and the O-band (1310 nm) for different phase change materials: GST [53], GSST [59],  $Sb_2S_3$  and  $Sb_2Se_3$ . \*Refers to a simulated value.

#### 4. CONCLUSIONS

In this paper, a MZI building block is demonstrated exploiting a novel family of low loss phase change materials in the telecommunications O and C-bands for future non-volatile electro-refractive modulation in programmable photonic integrated circuits in mid index waveguides. Losses lower than 0.09 dB/ $\mu m$  for  $Sb_2Se_3$  and 0.04 dB/ $\mu m$  for  $Sb_2S_3$  are demonstrated in both



ranges of the spectrum with changes in effective refractive index higher than 0.02. This study thus provides useful characterization information for the operation of non-volatile integrated photonic circuits based on phase change materials in two of the most important spectral ranges used for optical communications. The demonstration of these low loss non volatile building blocks, using a low loss and back end of the line compatible waveguide platform, have opened up pathways for more complex PIC's architecture and extended applications.

## Funding

Horizon 2020 Framework Programme (871391); Engineering and Physical Sciences Research Council (EP/M015130/1, EP/T007303/1, EP/R003076/1, EP/N00762X/1).

## Disclosures

The authors declare no conflicts of interest.

## References

1. X. Chen, M. M. Milosevic, S. Stanković, S. Reynolds, T. D. Bucio, K. Li, D. J. Thomson, F. Gardes, and G. T. Reed, "The emergence of silicon photonics as a flexible technology platform," *Proc. IEEE* **106**, 2101–2116 (2018).
2. M. Smit, K. Williams, and J. Van Der Tol, "Past, present, and future of inp-based photonic integration," *APL Photonics* **4**, 050901 (2019).
3. S. Khan, J. Chiles, J. Ma, and S. Fathpour, "Silicon-on-nitride waveguides for mid-and near-infrared integrated photonics," *Appl. physics letters* **102**, 121104 (2013).
4. J. Hong, A. M. Spring, F. Qiu, and S. Yokoyama, "A high efficiency silicon nitride waveguide grating coupler with a multilayer bottom reflector," *Sci. reports* **9**, 1–8 (2019).
5. A. Brimont, D. Thomson, P. Sanchis, J. Herrera, F. Gardes, J. Fedeli, G. Reed, and J. Martí, "High speed silicon electro-optical modulators enhanced via slow light propagation," *Opt. Express* **19**, 20876–20885 (2011).
6. D. J. Thomson, F. Y. Gardes, J. M. Fedeli, S. Zlatanovic, Y. Hu, B. P. P. Kuo, E. Myslivets, N. Alic, S. Radic, G. Z. Mashanovich, and G. T. Reed, "50-Gb/s silicon optical modulator," *IEEE Photonics Technol. Lett.* **24**, 234–236 (2012).
7. J. Faneca, B. T. Hogan, I. R. Diez, F. Y. Gardes, and A. Baldycheva, "Tuning silicon-rich nitride microring resonances with graphene capacitors for high-performance computing applications," *Opt. Express* **27**, 35129–35140 (2019).
8. Y.-Q. Bie, G. Grosso, M. Heuck, M. M. Furchi, Y. Cao, J. Zheng, D. Bunandar, E. Navarro-Moratalla, L. Zhou, D. K. Efetov *et al.*, "A mote 2-based light-emitting diode and photodetector for silicon photonic integrated circuits," *Nat. nanotechnology* **12**, 1124–1129 (2017).
9. F. Xia, T. Mueller, Y.-m. Lin, A. Valdes-Garcia, and P. Avouris, "Ultrafast graphene photodetector," *Nat. nanotechnology* **4**, 839–843 (2009).
10. Z. Zhou, B. Yin, and J. Michel, "On-chip light sources for silicon photonics," *Light. Sci. & Appl.* **4**, e358 (2015).
11. D. A. Miller, "Silicon photonics: Meshing optics with applications," *Nat. Photonics* **11**, 403–404 (2017).
12. L. Chrostowski, H. Shoman, M. Hammood, H. Yun, J. Khoja, E. Luan, S. Lin, A. Mistry, D. Witt, N. A. Jaeger *et al.*, "Silicon photonic circuit design using rapid prototyping foundry process design kits," *IEEE J. Sel. Top. Quantum Electron.* **25**, 1–26 (2019).
13. W. Bogaerts and L. Chrostowski, "Silicon photonics circuit design: methods, tools and challenges," *Laser & Photonics Rev.* **12**, 1700237 (2018).
14. W. Bogaerts, D. Pérez, J. Capmany, D. A. Miller, J. Poon, D. Englund, F. Morichetti, and A. Melloni, "Programmable photonic circuits," *Nature* **586**, 207–216 (2020).
15. K. E. Zinoviev, A. B. González-Guerrero, C. Domínguez, and L. M. Lechuga, "Integrated bimodal waveguide interferometric biosensor for label-free analysis," *J. lightwave technology* **29**, 1926–1930 (2011).
16. R. Wang, A. Vasiliev, M. Muneeb, A. Malik, S. Sprengel, G. Boehm, M.-C. Amann, I. Šimonytė, A. Vizbaras, K. Vizbaras *et al.*, "Iii-v-on-silicon photonic integrated circuits for spectroscopic sensing in the 2–4  $\mu\text{m}$  wavelength range," *Sensors* **17**, 1788 (2017).
17. C. Oton, C. Manganelli, F. Bontempi, M. Fournier, D. Fowler, and C. Kopp, "Silicon photonic waveguide metrology using mach-zehnder interferometers," *Opt. express* **24**, 6265–6270 (2016).
18. D. Pérez, I. Gasulla, L. Crudgington, D. J. Thomson, A. Z. Khokhar, K. Li, W. Cao, G. Z. Mashanovich, and J. Capmany, "Multipurpose silicon photonics signal processor core," *Nat. communications* **8**, 1–9 (2017).
19. D. Pérez, I. Gasulla, P. D. Mahapatra, and J. Capmany, "Principles, fundamentals, and applications of programmable integrated photonics," *Adv. Opt. Photonics* **12**, 709–786 (2020).
20. T. Rudolph, "Why i am optimistic about the silicon-photonic route to quantum computing," *APL Photonics* **2**, 030901 (2017).

21. X. Qiang, X. Zhou, J. Wang, C. M. Wilkes, T. Loke, S. O'Gara, L. Kling, G. D. Marshall, R. Santagati, T. C. Ralph *et al.*, "Large-scale silicon quantum photonics implementing arbitrary two-qubit processing," *Nat. photonics* **12**, 534–539 (2018).
22. S. Nandakumar, M. Le Gallo, I. Boybat, B. Rajendran, A. Sebastian, and E. Eleftheriou, "A phase-change memory model for neuromorphic computing," *J. Appl. Phys.* **124**, 152135 (2018).
23. I. Boybat, M. Le Gallo, S. Nandakumar, T. Moraitis, T. Parnell, T. Tuma, B. Rajendran, Y. Leblebici, A. Sebastian, and E. Eleftheriou, "Neuromorphic computing with multi-memristive synapses," *Nat. communications* **9**, 1–12 (2018).
24. T. H. Szymanski, "Securing the industrial-tactile internet of things with deterministic silicon photonics switches," *IEEE Access* **4**, 8236–8249 (2016).
25. Y. Zhou, S. Zheng, Z. Liu, T. Wen, Z. Ding, J. Yan, and G. Zhang, "Passive and active phase change materials integrated building energy systems with advanced machine-learning based climate-adaptive designs, intelligent operations, uncertainty-based analysis and optimisations: A state-of-the-art review," *Renew. Sustain. Energy Rev.* **130**, 109889 (2020).
26. A. Rahim, E. Ryckeboer, A. Z. Subramanian, S. Clemmen, B. Kuyken, A. Dhakal, A. Raza, A. Hermans, M. Muneeb, S. Dhoore *et al.*, "Expanding the silicon photonics portfolio with silicon nitride photonic integrated circuits," *J. lightwave technology* **35**, 639–649 (2017).
27. P. P. Absil, P. Verheyen, P. De Heyn, M. Pantouvaki, G. Lepage, J. De Coster, and J. Van Campenhout, "Silicon photonics integrated circuits: a manufacturing platform for high density, low power optical i/o's," *Opt. express* **23**, 9369–9378 (2015).
28. J. Klamkin, H. Zhao, B. Song, Y. Liu, B. Isaac, S. Pinna, F. Sang, and L. Coldren, "Indium phosphide photonic integrated circuits: Technology and applications," in *2018 IEEE BiCMOS and Compound Semiconductor Integrated Circuits and Technology Symposium (BCICTS)*, (IEEE, 2018), pp. 8–13.
29. H. Zhao, S. Pinna, F. Sang, B. Song, S. T. Š. Brunelli, L. A. Coldren, and J. Klamkin, "High-power indium phosphide photonic integrated circuits," *IEEE J. Sel. Top. Quantum Electron.* **25**, 1–10 (2019).
30. T. Domínguez Bucio, C. Lacava, M. Clementi, J. Faneca, I. Skandalos, A. Baldycheva, M. Galli, K. Debnath, P. Petropoulos, and F. Gardes, "Silicon Nitride Photonics for the Near-Infrared," *IEEE J. Sel. Top. Quantum Electron.* **26**, 1–13 (2019).
31. T. Domínguez Bucio, A. Z. Khokhar, G. Z. Mashanovich, and F. Y. Gardes, "N-rich silicon nitride angled MMI for coarse wavelength division (de)multiplexing in the O-band," *Opt. Lett.* **43**, 1251 (2018).
32. J. N. Milgram, J. Wojcik, P. Mascher, and a. P. Knights, "Optically pumped Si nanocrystal emitter integrated with low loss silicon nitride waveguides," *Opt. express* **15**, 14679–14688 (2007).
33. S. Gaugiran, S. Gétin, J. M. Fedeli, G. Colas, A. Fuchs, F. Chatelain, and J. Dérourard, "Optical manipulation of microparticles and cells on silicon nitride waveguides," *Opt. Express* **13**, 6956 (2005).
34. R. Baets, A. Z. Subramanian, S. Clemmen, B. Kuyken, P. Bienstman, N. Le Thomas, G. Roelkens, D. Van Thourhout, P. Helin, and S. Severi, "Silicon photonics: silicon nitride versus silicon-on-insulator," in *Optical Fiber Communication Conference*, (Optical Society of America, 2016), pp. Th3J–1.
35. X. Li, N. Youngblood, Z. Cheng, S. G.-C. Carrillo, E. Gemo, W. H. Pernice, C. D. Wright, and H. Bhaskaran, "Experimental investigation of silicon and silicon nitride platforms for phase-change photonic in-memory computing," *Optica* **7**, 218–225 (2020).
36. C. Ríos, M. Stegmaier, Z. Cheng, N. Youngblood, C. D. Wright, W. H. Pernice, and H. Bhaskaran, "Controlled switching of phase-change materials by evanescent-field coupling in integrated photonics," *Opt. Mater. Express* **8**, 2455–2470 (2018).
37. M. Wuttig, H. Bhaskaran, and T. Taubner, "Phase-change materials for non-volatile photonic applications," *Nat. Photonics* **11**, 465 (2017).
38. M. Wuttig and N. Yamada, "Phase-change materials for rewriteable data storage," *Nat. materials* **6**, 824–832 (2007).
39. R. Soref, "Tutorial: Integrated-photonics switching structures," *Apl Photonics* **3**, 021101 (2018).
40. G. Bruns, P. Merkelbach, C. Schlockermann, M. Salinga, M. Wuttig, T. Happ, J. Philipp, and M. Kund, "Nanosecond switching in GeTe phase change memory cells," *Appl. physics letters* **95**, 043108 (2009).
41. N. Ciocchini, M. Laudato, M. Boniardi, E. Varesi, P. Fantini, A. L. Lacaita, and D. Ielmini, "Bipolar switching in chalcogenide phase change memory," *Sci. reports* **6**, 29162 (2016).
42. P. Li, X. Yang, T. W. Maß, J. Hanss, M. Lewin, A.-K. U. Michel, M. Wuttig, and T. Taubner, "Reversible optical switching of highly confined phonon-polaritons with an ultrathin phase-change material," *Nat. materials* **15**, 870–875 (2016).
43. H. Y. Cheng, T. H. Hsu, S. Raoux, J. Y. Wu, P. Y. Du, M. Breitwisch, Y. Zhu, E. K. Lai, E. Joseph, S. Mittal, R. Cheek, A. Schrott, S. C. Lai, H. L. Lung, and C. Lam, "A high performance phase change memory with fast switching speed and high temperature retention by engineering the gexsbytez phase change material," in *2011 International Electron Devices Meeting*, (2011), pp. 3.4.1–3.4.4.
44. M. Stegmaier, C. Ríos, H. Bhaskaran, C. D. Wright, and W. H. Pernice, "Nonvolatile all-optical 1x2 switch for chipscale photonic networks," *Adv. Opt. Mater.* **5**, 1600346 (2017).
45. F. De Leonardis, R. Soref, V. M. Passaro, Y. Zhang, and J. Hu, "Broadband electro-optical crossbar switches using low-loss ge 2 sb 2 se 4 te 1 phase change material," *J. Light. Technol.* **37**, 3183–3191 (2019).
46. J. Feldmann, N. Youngblood, X. Li, C. D. Wright, H. Bhaskaran, and W. H. Pernice, "Integrated 256 cell photonic

- phase-change memory with 512-bit capacity,” *IEEE J. Sel. Top. Quantum Electron.* **26**, 1–7 (2019).
47. P. Xu, J. Zheng, J. K. Doylend, and A. Majumdar, “Low-loss and broadband nonvolatile phase-change directional coupler switches,” *ACS Photonics* **6**, 553–557 (2019).
  48. C. Ríos, M. Stegmaier, P. Hosseini, D. Wang, T. Scherer, C. D. Wright, H. Bhaskaran, and W. H. Pernice, “Integrated all-photonic non-volatile multi-level memory,” *Nat. Photonics* **9**, 725 (2015).
  49. N. Farmakidis, N. Youngblood, X. Li, J. Tan, J. L. Swett, Z. Cheng, C. D. Wright, W. H. Pernice, and H. Bhaskaran, “Plasmonic nanogap enhanced phase-change devices with dual electrical-optical functionality,” *Sci. Adv.* **5**, eaaw2687 (2019).
  50. E. Gemo, S. G.-C. Carrillo, C. R. De Galarreta, A. Baldycheva, H. Hayat, N. Youngblood, H. Bhaskaran, W. H. Pernice, and C. D. Wright, “Plasmonically-enhanced all-optical integrated phase-change memory,” *Opt. express* **27**, 24724–24737 (2019).
  51. Z. Cheng, C. Ríos, W. H. Pernice, C. D. Wright, and H. Bhaskaran, “On-chip photonic synapse,” *Sci. advances* **3**, e1700160 (2017).
  52. J. Feldmann, N. Youngblood, C. Wright, H. Bhaskaran, and W. Pernice, “All-optical spiking neurosynaptic networks with self-learning capabilities,” *Nature* **569**, 208–214 (2019).
  53. J. Faneca, S. G.-C. Carrillo, E. Gemo, C. R. de Galarreta, T. D. Bucio, F. Y. Gardes, H. Bhaskaran, W. H. Pernice, C. D. Wright, and A. Baldycheva, “Performance characteristics of phase-change integrated silicon nitride photonic devices in the o and c telecommunications bands,” *Opt. Mater. Express* **10**, 1778–1791 (2020).
  54. Y. Zhang, J. Li, J. Chou, Z. Fang, A. Yadav, H. Lin, Q. Du, J. Michon, Z. Han, Y. Huang *et al.*, “Broadband transparent optical phase change materials,” in *CLEO: Applications and Technology*, (Optical Society of America, 2017), pp. JTh5C–4.
  55. M. Miscuglio, J. Meng, O. Yesiliurt, Y. Zhang, L. J. Prokopeva, A. Mehrabian, J. Hu, A. V. Kildishev, and V. J. Sorger, “Artificial synapse with mnemonic functionality using gsst-based photonic integrated memory,” in *2020 International Applied Computational Electromagnetics Society Symposium (ACES)*, (IEEE, 2020), pp. 1–3.
  56. Y. Zhang, J. B. Chou, J. Li, H. Li, Q. Du, A. Yadav, S. Zhou, M. Y. Shalaginov, Z. Fang, H. Zhong *et al.*, “Broadband transparent optical phase change materials for high-performance nonvolatile photonics,” *Nat. communications* **10**, 1–9 (2019).
  57. W. Dong, H. Liu, J. K. Behera, L. Lu, R. J. Ng, K. V. Sreekanth, X. Zhou, J. K. Yang, and R. E. Simpson, “Wide bandgap phase change material tuned visible photonics,” *Adv. Funct. Mater.* **29**, 1806181 (2019).
  58. M. Delaney, I. Zeimpekis, D. Lawson, D. W. Hewak, and O. L. Muskens, “A new family of ultralow loss reversible phase-change materials for photonic integrated circuits: Sb<sub>2</sub>S<sub>3</sub> and Sb<sub>2</sub>Se<sub>3</sub>,” *Adv. Funct. Mater.* **30**, 2002447 (2020).
  59. J. Faneca, L. Trimby, I. Zeimpekis, M. Delaney, D. W. Hewak, F. Y. Gardes, C. D. Wright, and A. Baldycheva, “On-chip sub-wavelength bragg grating design based on novel low loss phase-change materials,” *Opt. Express* **28**, 16394–16406 (2020).
  60. Z. Fang, J. Zheng, and A. Majumdar, “Non-volatile integrated photonics enabled by broadband transparent phase change material,” in *CLEO: Applications and Technology*, (Optical Society of America, 2020), pp. JTh2B–3.
  61. T. Domínguez Bucio, A. Z. Khokhar, C. Lacava, S. Stankovic, G. Z. Mashanovich, P. Petropoulos, and F. Y. Gardes, “Material and optical properties of low-temperature NH<sub>3</sub>-free PECVD SiN<sub>x</sub> layers for photonic applications,” *J. Phys. D: Appl. Phys.* **50** (2017).
  62. C. Ríos, P. Hosseini, C. D. Wright, H. Bhaskaran, and W. H. Pernice, “On-chip photonic memory elements employing phase-change materials,” *Adv. Mater.* **26**, 1372–1377 (2014).
  63. H. Zhang, L. Zhou, B. M. A. Rahman, X. Wu, L. Lu, Y. Xu, J. Xu, J. Song, Z. Hu, L. Xu, and J. Chen, “Ultracompact si-gst hybrid waveguides for nonvolatile light wave manipulation,” *IEEE Photonics J.* **10**, 1–10 (2018).